



Synthesizing and Characterizing the Hybrid Pigment $\text{Fe}_{0.7}\text{Cr}_{1.3}\text{O}_3$ With High NIR Reflectance for Sustainable Energy Saving Applications

Gh. Mobarhan¹, A. Souri^{*1}, S. K. Seyed Mostafavi², M. Ghahari^{**2}, M. Safi³

¹ Department of Materials Engineering, Faculty of Engineering, Malayer University, P. O. box: 65741-84621, Malayer, Iran

² Department of Nano Materials and Nano Coatings, Institute for Color Science and Technology, P. O. Box: 16765-654, Tehran, Iran

³ Department of Color physics, Institute for Color Science and Technology, P. O. Box: 16765-654, Tehran, Iran

ARTICLE INFO

Article history:

Received: 02 Jan 2022

Final Revised: 04 Apr 2022

Accepted: 05 Apr 2022

Available online: 07 June 2022

Keywords:

Cool nano pigments

Reflected near-infrared radiation

Surfactant

Morphology

$\text{Fe}_{0.7}\text{Cr}_{1.3}\text{O}_3$

Hydrothermal synthesis

ABSTRACT

Today, a growing number of the world population faces a rise in the cost of living significantly increased energy costs. That is why Energy-saving has become a vital issue. One of the remarkable ways to reduce energy consumption is using cool pigments; therefore, research has been done to improve pigments' infrared reflection capability. In this paper, the role of particle morphology was investigated to boost the infrared reflection property of iron-chromium-based pigments. For this purpose, a series of inorganic pigments based on the $\text{Fe}_{0.7}\text{Cr}_{1.3}\text{O}_3$ formula was prepared via a hydrothermal method. Surfactants altered the particles' morphology to improve the pigments' reflecting properties. According to the IR reflectance results, flaky particles exhibit an enhanced IR reflection, and they have significantly larger IR reflections than spherical particles. Furthermore, the results have revealed that silica coating leads to a meaningful improvement in the IR reflection property. It was found that the maximum near-infrared solar reflectance of the sample with 2.63 % succinic acid surfactant and silica coating was 52.23 % compared to that of $\text{Fe}_{0.7}\text{Cr}_{1.3}\text{O}_3$, which was 25.36 %. Prog. Color Colorants Coat. 15 (2022), 341-353© Institute for Color Science and Technology.

1. Introduction

Nowadays, reducing energy consumption has become a vital issue for developed countries. There is a growing tendency amongst people to reduce energy costs. Although there are many ways to reduce domestic energy usage, applying cool colors is one of the most effective [1-4]. These cool colors could be used as coatings on the house roofs and effectively reflect the sunlight's infrared part. The cool pigments play a prominent role in these cool coatings [5, 6]. Many researchers have focused on these pigments during the last years to improve their IR reflectance property [7-

11]. The coating reflectance depends on the pigment reflecting index, pigment particle size, particle size distribution, particle morphology, crystallite size, compaction density, and pigment volume concentration. Pigment reflecting index and particle size play the most significant roles [12].

Kiomarsipour et al. [13] investigated the effect of ZnO's particle size and pigment morphology on infrared reflectance. Based on this research, the nano and micro-rod, scale-like, and nanoparticle-decorated ZnO pigments had shown lower to higher reflectance spectra, respectively. The presence of nanoparticles on the scale-

*Corresponding author: asouri@malayeru.ac.ir

**maghahari@icrc.ac.ir

like particles increased infrared reflectance due to the increase in the particles' specific surface area and surface roughness, leading to enhanced light scattering efficiency. Zhi et al. [14, 15] synthesized antimony oxide nanoparticles via the hydrothermal method using CTAB. The reflectance of flower-like nanoparticles was higher than that of wire and spherical nanoparticles. Thongkanluang et al. [16, 17] synthesized inorganic green and brown pigments based on chromium or iron oxide with a high infrared reflectance via the host-guest method. The best composition was obtained with 46.7 % reflectance. Although several types of research have been performed on the infrared reflecting property of $(\text{Fe}, \text{Cr})_2\text{O}_3$ [18, 19], there is no research study on the NIR reflectance property of $\text{Fe}_{0.7}\text{Cr}_{1.3}\text{O}_3$ pigment, but our recently published work [20]. In this paper, we synthesized $\text{Fe}_{0.7}\text{Cr}_{1.3}\text{O}_3$ pigments by the co-precipitation method, and the NIR reflectance was enhanced by applying titanium dioxide coating on the pigment. Furthermore, the NIR solar reflectance property of brown pigments with structures except iron oxide has been investigated. J. Zou et. al.[21] and L. Liu et al. [22] have studied the NIR properties of Cr-doped CaTiO_3 and Mg-doped ZnFe_2O brown pigments and obtained NIR solar reflectance of 58 and 51 %, respectively.

In the present study, the $\text{Fe}_{0.7}\text{Cr}_{1.3}\text{O}_3$ pigments were synthesized via the hydrothermal method. Our previous series of tests selected the base pigment used in this study. The morphology of particles has a stimulating effect on NIR reflectance; therefore, the morphology was altered by utilizing the different surfactants during the synthesis procedure. The simultaneous influence of silica coating and morphology of particles has not been studied yet. Therefore, this paper examined the effects of morphology and silica coating on the particles' infrared reflectance.

2. Experimental

2.1. Materials

Non-hydrated iron nitrate ($\text{Fe}(\text{NO}_3)_3$, Merck, 99.0 %), non-hydrated chromium nitrate ($\text{Cr}(\text{NO}_3)_3$, Merck, ≥ 99.0 %), ethanol (Merck, 99.5 %), and NaOH (Merck, 28.0 %) were used as precursors for synthesizing $\text{Fe}_{0.7}\text{Cr}_{1.3}\text{O}_3$ particles. Also, sodium dodecyl sulfate (SDS, $\text{CH}_3(\text{CH}_2)_{11}\text{SO}_4\text{Na}$, Merck), succinic acid ($\text{C}_4\text{H}_6\text{O}_4$, Merck), cetyltrimethylammonium bromide (CTAB, $\text{C}_{19}\text{H}_{42}\text{BrN}$, Merck), and L-cysteine ($\text{C}_3\text{H}_7\text{NO}_2\text{S}$, Merck) were used as surfactants to control

the morphology of the particles. Furthermore, tetraethyl orthosilicate (TEOS, Merck, ≥ 98 %) was used as the silica source for coating $\text{Fe}_{0.7}\text{Cr}_{1.3}\text{O}_3$ particles. The chemicals were utilized without further purification.

2.2. Pigment preparation

The hydrothermal process was used to synthesize $\text{Fe}_{0.7}\text{Cr}_{1.3}\text{O}_3$ particles, and the procedure was as follows. Initially, based on an assumed molecular formula for $\text{Fe}_{0.7}\text{Cr}_{1.3}\text{O}_3$, 1 g of non-hydrated iron nitrate and 2 g of non-hydrated chromium nitrate (Fe/Cr molar ratio of 1:2) were separately dissolved in 10 mL distilled water. Then, a specific amount of surfactant was added to the solution. The samples were synthesized with four different surfactant concentrations regarding their CMC points. After mixing the precursors in water, the proper amount of NaOH (0.25 M) was added to adjust the pH to 9. The mixture was transferred to a 40 mL autoclave vessel and then heated in the oven at 180 °C for 3 h. After cooling the vessel down, the suspension was centrifuged at 2000 rpm to obtain the product. It was rinsed three times with distilled water and ethanol. The pH was neutralized, and the product was dried at 70 °C. It was then heated in a furnace at 800 °C for 1 h with a rate of 10 °C/min.

Furthermore, three samples were synthesized in the presence of TEOS to investigate the effect of silica on the near-IR reflectance. Samples with 0.129, 0.258, and 0.387 wt% TEOS were labeled DS7, DS8, and DS9. For this purpose, TEOS was added to the solution containing both chromium and iron nitrate. These pigments were prepared according to the procedure mentioned above for the pigment without TEOS.

2.3. Characterization

X-ray diffraction (XRD) patterns of the powder samples were recorded using $\text{CuK}\alpha$ radiation (1.54056 Å) on a Philips X-ray diffractometer (Philips PW 3710). The primary crystallite size was calculated using the Scherrer equation ($d=0.9\lambda/\beta \cos \theta$). The morphology and particle size of the as-synthesized powders were studied by scanning electron microscopy (SEM, TE-SCAN, Model MIRA 3) and transmission electron microscopy (TEM, Philips Em208). The size of at least 100 particles in each SEM image was measured by Digimizer software. Fourier Transform

Infrared (FTIR) spectroscopy was also performed using Bruker equipment (Vector-33 model). Powder samples were mechanically pressed to obtain disk-shaped samples with a diameter of 1.5 cm and thickness of 2 cm to investigate the infrared reflectance. Spectral reflectance data were used to calculate the NIR solar reflectance of Fe_{0.7}Cr_{1.3}O₃ sample. Their reflectance was obtained using NIR Quest 256-2.5 (Array-based 900-2500) UV-VIS-NIR spectrophotometer in the wavelength range of I1 (700 nm) to I2 (2500 nm). The calculation was fulfilled by weighted averaging using a standard solar spectrum (ASTM G159-98) as the weighting function (Eq. 1) [23]:

$$R^* = \frac{\int_{\lambda_1}^{\lambda_2} r(\lambda) i(\lambda) d\lambda}{\int_{\lambda_1}^{\lambda_2} i(\lambda) d\lambda} \quad (1)$$

where $r(\lambda)$ is the spectral reflectance collected from the experiment, and $i(\lambda)$ is the standard solar spectrum ($\text{W m}^{-2} \mu\text{m}^{-1}$).

The pressed samples were used for color measurement analysis. The values of CIE-L*a*b* were computed under a D65 illuminant and CIE 1964 (10°) standard observer. Spectral reflectance and color features (*b*a* L CIE) were obtained by S1000 spectrophotometer (Konica Minolta, CM-2300d) in 400-700 nm.

3. Results and Discussion

3.1. The effect of surfactant on the NIR reflectance of the powder pigments

The diffraction patterns of the samples calcined at 800 °C are shown in Figure 1. The patterns could be assigned to Chromium Iron Oxide (Fe_{0.7}Cr_{1.3}O₃) with a

rhombohedral crystal system (JCPDS card no: 00-035-1112). As can be seen, the surfactant has no significant effect on the final phase, and the peaks of all four samples synthesized in the presence of surfactant are identical to those of the reference sample. Also, the diffraction pattern of the G sample before calcination is shown in Figure 1. No remarkable peaks were observed in the G sample. It could be recognized that the crystallinity does not complete after the hydrothermal process. The primary crystallite size was calculated from the half-height width (β) of the three prominent peaks ((104), (110), and (116)) of Fe_{0.7}Cr_{1.3}O₃ phase using the Scherrer equation ($d = 0.9\lambda/\beta \cos \theta$). It is listed in the inset of Figure 1. The calculated primary crystallite size of the G sample is 33.8 nm. The crystallite size in the (104) plane reached 20.6, 42.1, 24.1, and 24.1 nm after adding an optimum CTAB, SDS, succinic acid, and L-Cysteine, respectively. The XRD results revealed a suitable phase for all the samples were obtained.

The morphology of the G sample is shown in Figure 2. Most particles have a semispherical morphology. However, shapeless or irregular morphologies are also seen in the SEM image. The particle size distribution ranges from 50 to 250 nm. Figures 2 shows FESEM image of samples that are synthesized in the presence of CTAB. The morphology of C series samples did not change remarkably in comparison with sample G. It seems that the particles are round and almost have spherical morphology. However, the particle size distribution in the C series has a narrower distribution comprising sample G. There are no significant differences in morphology between C1 and C2 samples.

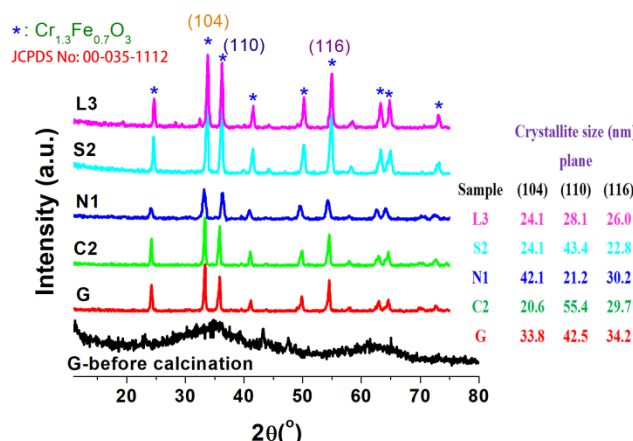


Figure 1: The XRD patterns of samples, Inset shows the primary crystallite size of the particles.

Meanwhile, the particle size of sample C3 has significantly increased by doubling the amount of surfactant compared with sample C2. SDS concentration showed a different effect on the morphology of the particles. Figures 2a show the SEM images of the N series samples. Plate-like particles with a thickness of 125 and a diameter of 250 nm were formed at low SDS concentrations (N1 sample). The uniformity of the particles was remarkable; however, more spherical morphology was observed by increasing the SDS concentration.

Moreover, the diameter of the particles was reduced by increasing SDS concentration. The diameter of the particle in the N4 sample reaches about 100 nm. The mentioned conditions are entirely different for samples in the S series samples. Succinic acid completely changed the morphology of the particles at different surfactant concentrations. Figures 1C shows the SEM images of the S series samples. At low succinic acid concentration (S1 sample), several plate-like particles

with a thickness of ~200 nm and a diameter of ~500 nm were formed; however, some small particles had semispherical morphology. As the concentration of succinic surfactant was increased, these small particles diminished or adhered to the surface of bigger particles, forming giant flake-like particles. In sample S2, the morphology is more or less flaky; nevertheless, the flake thickness is significantly bigger than S1. The mean size and thickness of the flakes are less than 1 micron and 400 nm, respectively. In sample S3, the flake size increases, and the thickness decreases compared to S2.

Figures 2d shows the SEM images of L1 and L3 samples. The morphology of the particles is spherical. No morphology changes are observed in the particles of these samples; however, the size of the particles is remarkably increased by raising the surfactant concentration. The average size of the particles in the sample L3 is about 130 nm.

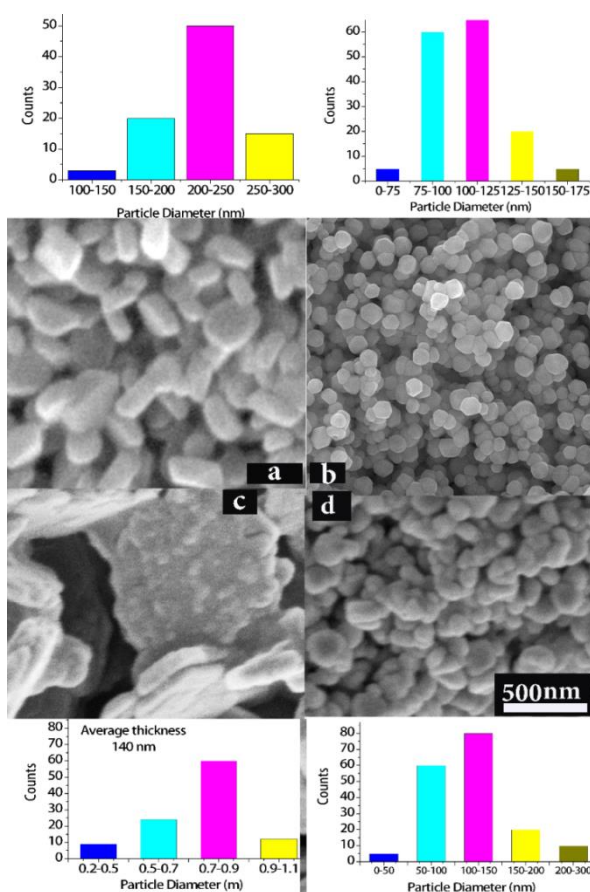


Figure 2: SEM images and particle size distribution of samples synthesized in the presence of different surfactants, a:N1, b:C2, c:S2, and d: L2.

Depending on its structure, each surfactant strongly affects the synthesized particles' morphology. The anionic surfactant (succinic acid) yields flaky particles, while the cationic surfactant (CTAB) tends to form spherical particles [24, 25]. In general, altering the primary crystal size is based on the thermodynamic (surface energy change) and the kinetic (suppression of crystal growth with capping) effects. Here succinic acid has a remarkable influence on particle morphology. As can be seen in the inset of Figure 1 and based on primary size at different planes ((104), (110), and (116)), it seems that the molecules of surfactant attach on (104) and (116) planes to lower their energy and simultaneously suppress the crystal growth in (110) plane. Therefore, it could be concluded that the final particle size resembles the primary crystal morphology. The particles' aspect ratio was increased by increasing the succinic acid concentration and then decreased [26, 27]. The surfactant's nature can affect the crystal habit by selective adsorption processes leading to preferential growth inhibition for distinct crystal planes. Additional strong, attractive interactions between the surfactant and the inorganic surface can arrest the nucleation and change the primary clusters' shape and size [28].

Figure 3 presents the changes in the NIR reflectance of some samples. The highest reflectance belongs to S2, in which thin flakes were grown beside each other in different angles and directions. Among the samples with spherical particles, those which have smaller particles showed higher reflectance. L4 shows the lowest reflectance between all samples. Among the

used surfactants, succinic acid possesses the best performance. Particles synthesized with this surfactant revealed flaky particles. Comparing SEM images and the samples' reflectance indicates that the flake morphology remarkably increases the reflectance [29, 30]. Interestingly, as seen in Figure 3, although S2 and N2 samples have more or less similar colors, their NIR reflection is remarkably different. Therefore, it could be concluded that the structure of the sample (particle size and morphology) significantly affects NIR reflection.

3.2. The effect of coating on the NIR reflectance of the powder pigment

In the previous section, succinic acid significantly affected the morphology, leading to higher IR reflectance. Therefore, to investigate the effect of silica coating on IR reflectance, 2.64 wt% succinic acids were selected with TEOS.

Figure 4 (a, b, and d) represents SEM images of DS9 at different magnifications. The sample compared to sample S2 has thinner flake-like particles. The average thickness of these flakes is less than 100 nm. The flakes seem to be formed individually compared to the samples without silica. Therefore, it could be concluded that TEOS contributes to modifying the morphology during the hydrolysis process. SEM results obtained for DS7 and DS8 support this idea too. The flaky particles of sample DS7 were stuck to each other. The number of individual flakes was formed more by increasing the TEOS in the DS8 sample.

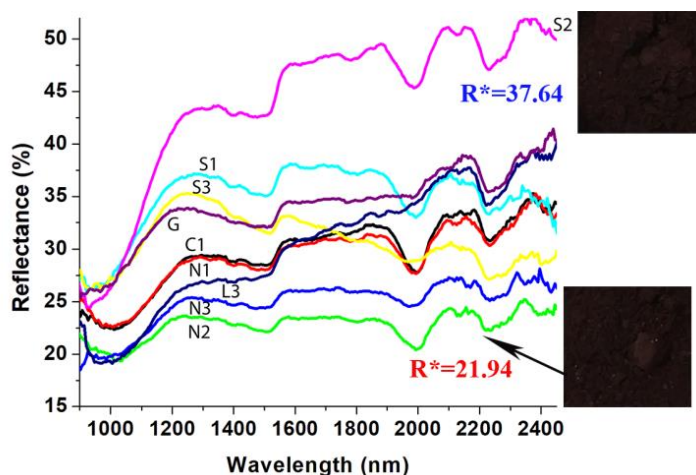


Figure 3: NIR reflectance of samples in the presence and absence of surfactant.

Consequently, the role of TEOS as a co-surfactant could not be negligible. It seems that Si(OH)_x molecules have an impressive effect on forming homogenous flaky-like morphology. TEOS is hydrolyzed to Si(OH)_x species during the synthesis process; it controls the electrostatic interaction between $(\text{FeCr})\text{OH}$ species and the anionic part of succinic acid [28], so thinner $(\text{FeCr})\text{OH}$ seeds are obtained. Figure 5 schematically shows the growth of the pigments in the presence of TEOS.

Figure 4c was taken in backscatter mode. There is no significant contrast in the image, implying that a single-phase sample is probably obtained. The images reveal that these elements are homogeneously distributed throughout the particles. The linear analysis was utilized at 10 points to investigate the precise amounts of these elements. The ratio of Cr/Fe is almost constant over the analyzed line and represents the $\text{Fe}_{0.7}\text{Cr}_{1.3}\text{O}_3$ formula. The probability of the entrance of Si ions into the $\text{Fe}_{0.7}\text{Cr}_{1.3}\text{O}_3$ structure is very low due to

the remarkable differences between ions radii of Si (54 pm) and Fe (69 pm) or Cr (75.5 pm). Therefore, it could be deduced that Si(OH)_x molecules covered the primary particles of $(\text{FeCr})_x(\text{OH})_x$ during the synthesis process. Then, it will be converted to SiO_2 after the calcination process.

Furthermore, TEM images of DS9 suggest that SiO_2 covered the particles as a coating rather than forming individual silica particles. A flaky-like particle can be seen in Figure 6a. It seems that the particle includes some tiny flakes. The inset in Figure 6 represents the EDX taken from the SEM image, which indicates the presence of Si, O, Cr, and Fe elements. The weight percentage ratio of Cr, Fe, and O resembles the $\text{Fe}_{0.7}\text{Cr}_{1.3}\text{O}_3$ formula. TEM image (Figure 6b) proves that each flake consists of tiny flakes. In Figure 6c, the edge of a particle is shown at a higher magnification. As can be seen, the lattice fringes are visible at the outer layer, which is identified by a circle in the image.

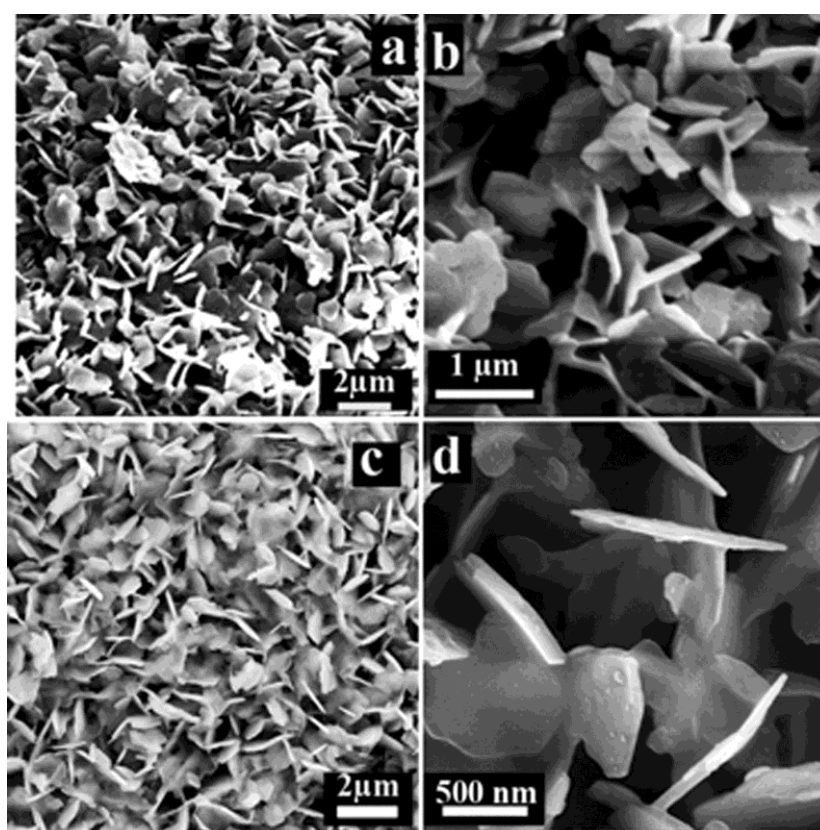


Figure 4: a, b and d) SEM images of DS9 sample at different magnifications, c) backscatter mode.

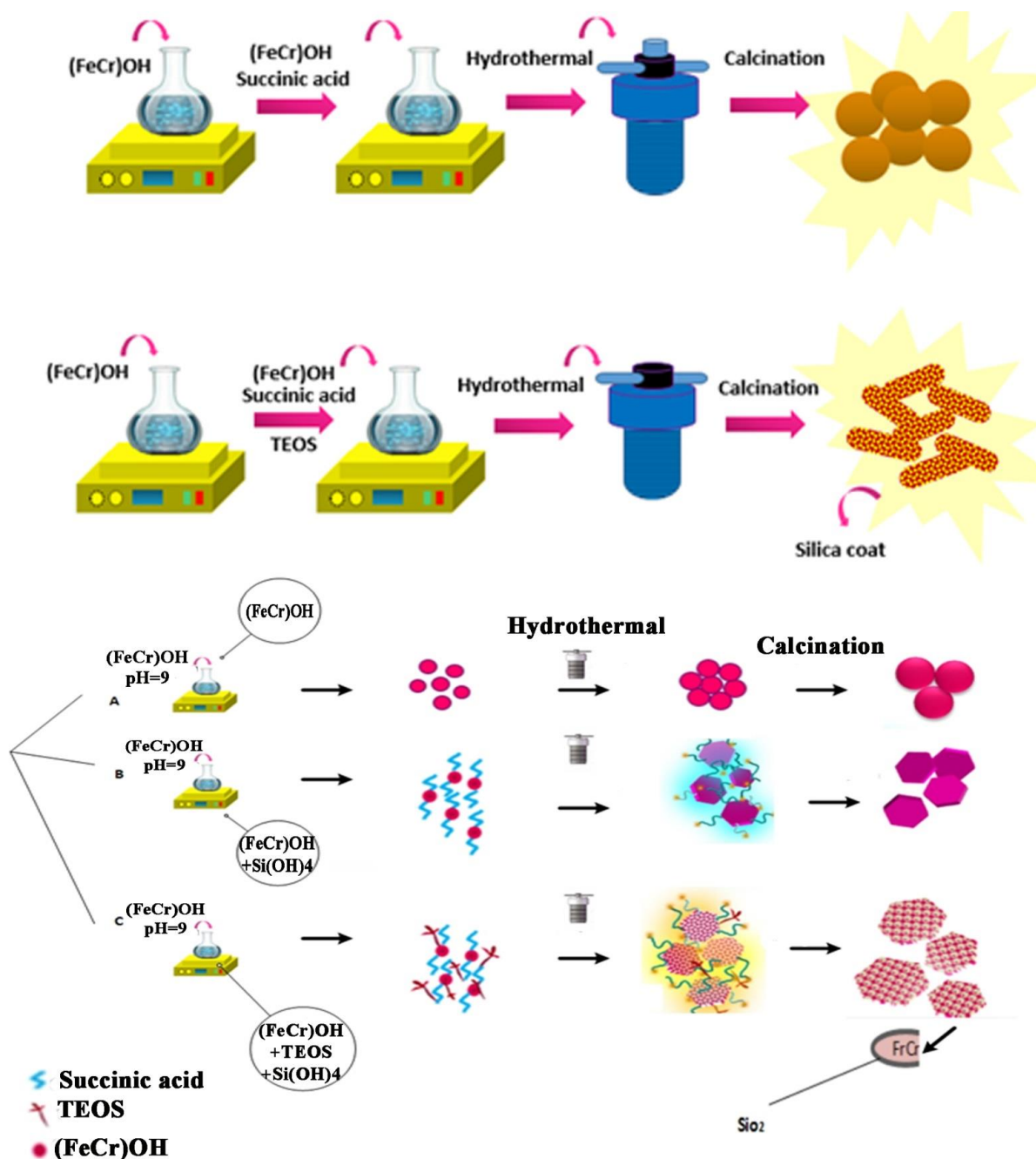


Figure 5: Schematic growth of flaky pigment in the presence of TEOS and succinic acid A) without addition B) including Succinic Acid C) including Succinic Acid and TEOS.

Furthermore, Figures 6d and 6e show a particle's selected area electron diffraction (SAED) patterns. The ring pattern obtained at the edge region and bulk confirms the samples' crystalline nature, following the XRD patterns. XRD analysis was performed to reveal whether silica coating is amorphous or crystalline. The diffraction pattern of G and DS9 samples, calcined at 800 °C. The crystal structure of this phase is Rhombohedral (JCPDS card no. 00-035-1112). The

ionic radius of Si (54 pm) is smaller than Fe (69 pm) and Cr (75.5 pm), and there is not a distinguishable peak shift in the pattern. It clarifies that there is no significant shift in the peak location. So, doping could not be happened [31]. No amorphous phase can be seen in DS9. There is, however, a small peak at $2\theta=22^\circ$ that can be related to the cristobalite phase (SiO_2). The sample was heat-treated at 1000 °C to find more detailed information. In this situation, the peak at

$2\theta=22$ indicates a remarkable increase in crystallinity [32]. TEM diffraction results (shown in Figure 6e) confirm the covering particles and silica crystallinity. There is, however, a small peak at $2\theta=22^\circ$ that can be related to the cristobalite phase (SiO_2).

The only significant peak in the sample at 600 cm^{-1} is related to the metal bond between chromium and iron with oxygen. According to the literature, the spinel-type compounds show two bands in the $550\text{--}650\text{ cm}^{-1}$ region assigned to the vibration of metal-oxygen bonds [33]. Generally, this spectrum is similar to that of the G sample, except that another peak is observed at 1000 cm^{-1} . This peak can be attributed to the Si-O-Si

bond [34]. The comparison of FTIR spectra of G and DS9 samples reveals that silica has not been separately created in the system and has covered the surface of $\text{Fe}_{0.7}\text{Cr}_{1.3}\text{O}_3$ particles because the peak related to $(\text{Fe-O})=578$ has shifted to 557 cm^{-1} [35]. The peak at 1015 cm^{-1} is related to Si-O-Si stretching vibrations, suggesting that silica has formed on the particles.

Furthermore, there is no evidence of peaks at $850\text{--}960\text{ cm}^{-1}$ which belong to Si-OH asymmetric bending and stretching vibration. These observations are well documented and are attributed to the successful coating of Fe_3O_4 nanoparticles by silica [36]. These results confirm TEM observations too.

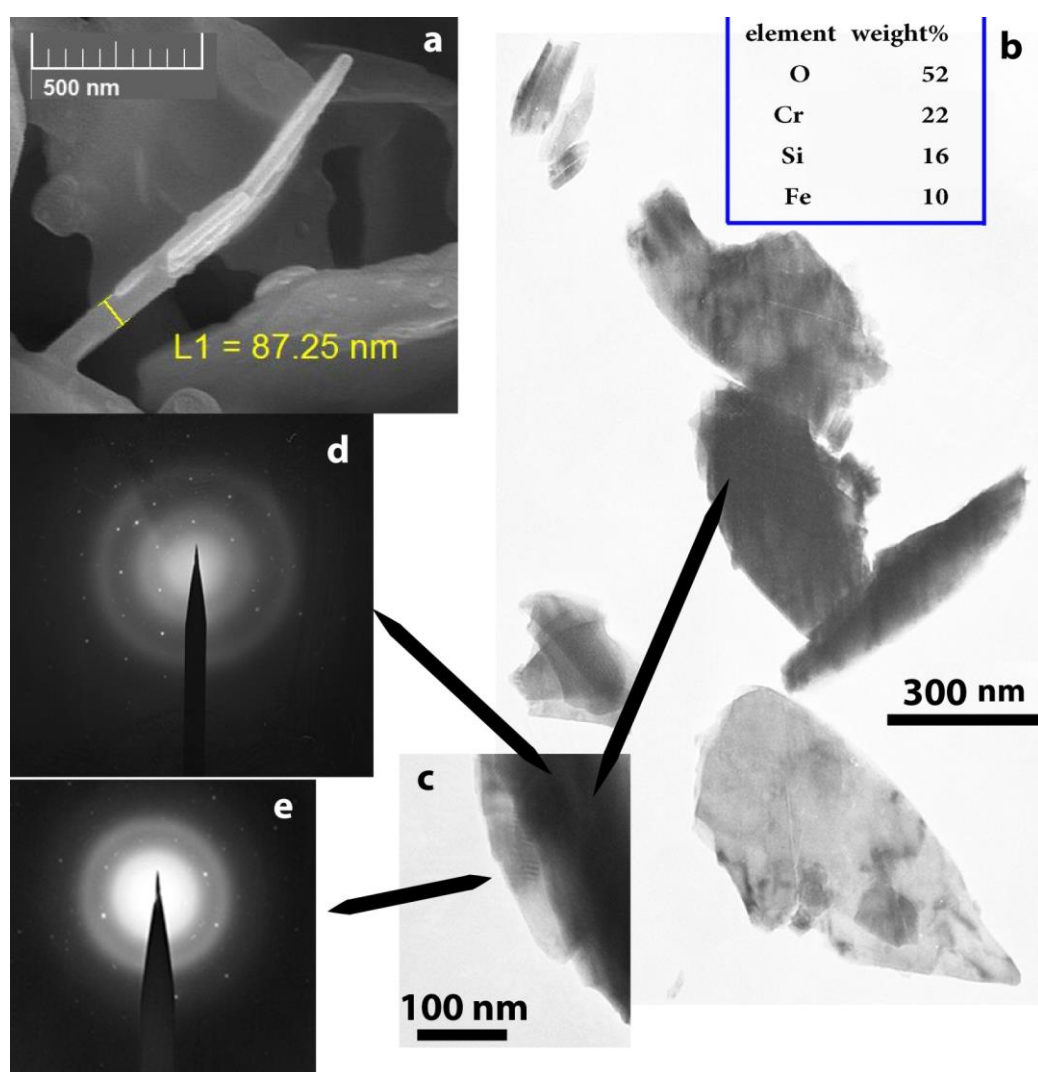


Figure 6: SEM (a) and TEM micrographs (b and c) and SAED (d and e) patterns of the DS9 sample.

In Figure 7a, the infrared reflectance spectra of the samples are depicted. The highest reflectance belongs to the DS9 sample. Due to the difference in reflecting indices between the silica layer and $\text{Fe}_{0.7}\text{Cr}_{1.3}\text{O}_3$ particle, adding more Si has resulted in a 10 % increase in infrared reflectance. Another reason for the high infrared reflectance of this sample is the composition of flakes thinner than 50 nm. The infrared rays are continuously scattered when hitting these flakes, preventing rays from penetrating the underlying layers [14]. Furthermore, silica creates a glassy layer on the particles and reflects infrared rays [37]. Son et al. reported that the core-shell structure consisting of a low refractive index core and high refractive index shell provides efficient light scattering [38].

The NIR reflection of the calcined and uncalcined samples was also analyzed, and the results are represented in Figure 7a. Although they have more or less similar colors, the uncalcined sample showed weak reflection compared to the calcinated one. By comparing the X-ray diffraction patterns (Figure 7b) and UV/Vis absorption spectra of the samples, it could be concluded that the crystalline phase may boost the NIR reflection. Furthermore, the crystallite and particle size of the sample will be grown by the calcination process. The bandgap energy increases by the calcination process, too, probably due to the increase in the particle size of the calcined sample. The reflectance mechanism in the G and DS9 samples is schematically illustrated in Figure 8.

Ge et al. reported that the IR reflectance of nanosheets and orderly flower-like microstructures of Sb_2O_3 is remarkably higher than that of Sb_2O_3 nanowires and powders [14]. In some research, titanium dioxide

was applied as a composite or coating to enhance the NIR reflection property. We demonstrated in our last work that $(\text{Fe}, \text{Cr})_2\text{O}_3@\text{TiO}_2$ has shown higher NIR reflectance than $(\text{Fe}, \text{Cr})_2\text{O}_3\text{-TiO}_2$ solid solution due to its core-shell structure with different refractive indices [20]. Thongkanluang et al. reported that complex inorganic brown pigment with high NIR reflectance (41 %) was synthesized by taking Fe_2O_3 , Sb_2O_3 , SiO_2 , and Al_2O_3 . The NIR reflectance reached 46.7 % By adding 6 wt% TiO_2 [39]. Also, some researchers promoted the NIR reflectance of pigments in the doping process. Liu et al. obtained over 51 % NIR reflectance by doping magnesium in zinc ferrite series [22]. Zou et al. synthesized dark brown pigment based on CaTiO_3 doped with 1 wt% Cr. This pigment showed high NIR solar reflectance (58 %) [21]. We could enhance the NIR reflectance of iron chromate brown pigment from 25 to 52 % by altering the morphology and applying the silica shell.

Color variations are measured by the distance between two points in CIE LAB. The color measurement data presented in Figure 9 and Tables 1 reveal remarkable changes in color in most samples, especially DS7, DS9, and S4. Although the color difference value (ΔE^*) is relatively high for the DS7 sample, the main difference between G and DS7 samples comes from dissimilarity in their lightness values (ΔL^*). Therefore, it could be concluded that DS9 is somewhat darker than the G sample [40]. As shown in Table 1, there is no notable trend between ΔE^* and IR reflectance. However, the obtained results indicate no remarkable color difference between DS9 and G samples, the color of some samples, such as DS7 and S4 altered by using surfactant during the synthesis.

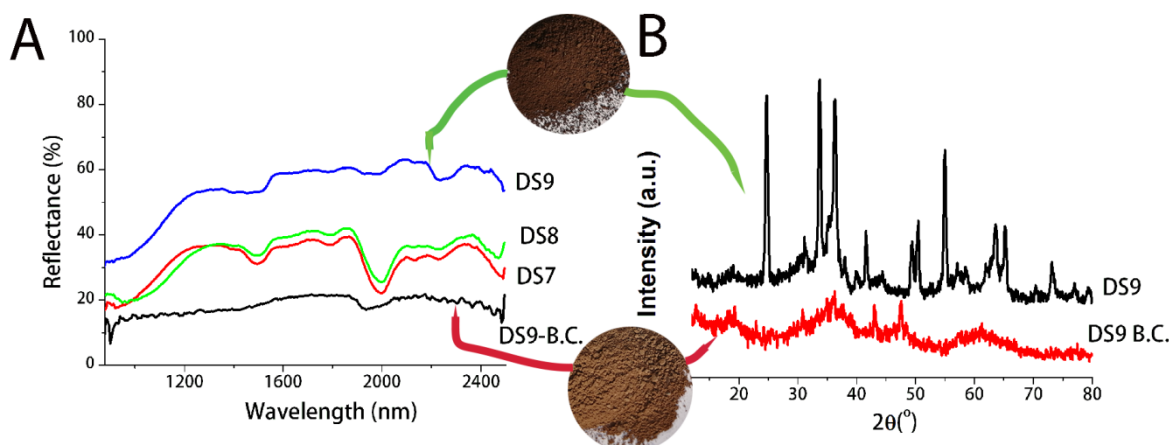


Figure 7: The NIR reflectance of samples after calcination at 800 °C.

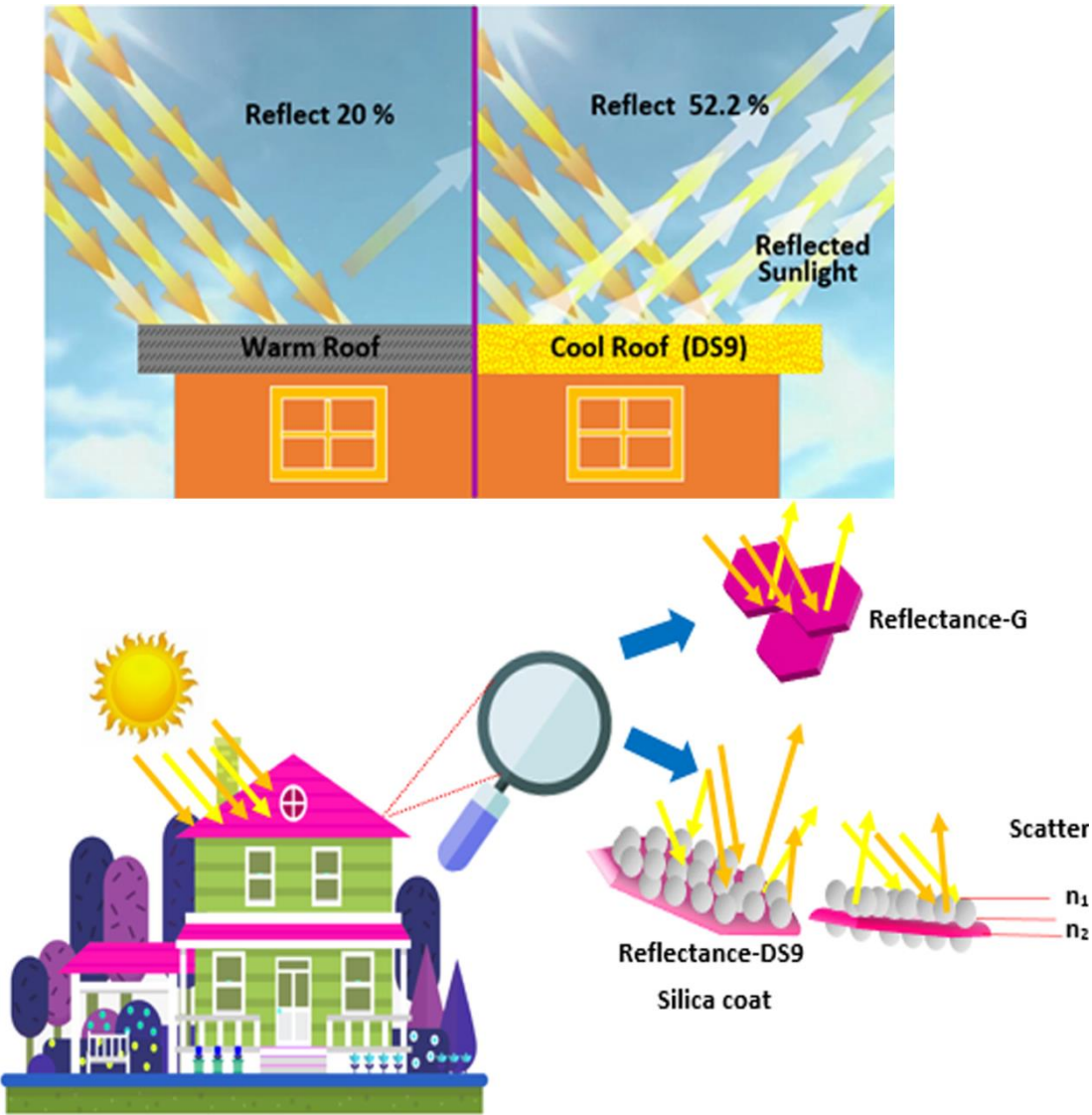


Figure 8: The reflectance mechanism in the DS9 sample.

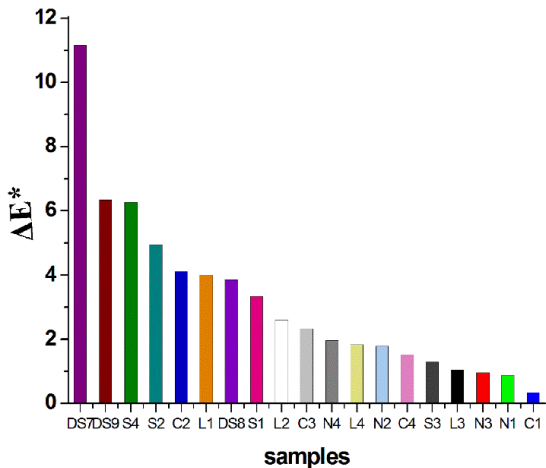


Figure 9: Color differences values between G (reference) and other samples.

Table 1: NIR solar reflectance and color coordinate of samples.

Sample	ΔL^*	Δa^*	Δb^*	Δc^*	Δh^0	R*
S1	3.27	0.7	0.25	0.72	-1.69	33.25
S2	3.86	-2.57	-1.75	-3.1	1.13	37.64
S3	1.05	0.69	0.3	0.74	-1.28	30.92
S4	4.35	-4.18	-1.68	-4.09	30.29	25.15
C1	-0.23	0.21	0.16	0.27	0.07	24.79
C2	1.14	-2.42	3.12	1.02	33.29	26.90
C3	-1.16	1.19	1.64	1.95	4.52	22.4
C4	1.42	-0.15	0.54	0.22	4.69	19.17
N1	-0.3	0.84	0.02	0.71	-3.94	26.83
N2	-0.53	1.4	1	1.73	-0.02	21.94
N3	0.84	0.31	0.36	0.46	0.98	23.4
N4	1.13	0.8	1.4	1.5	5.02	21.74
L1	2.2	1.79	2.82	3.18	7.74	25.06
L2	2.27	-0.28	1.25	0.6	10.05	23.74
L3	0.82	-0.58	-0.28	-0.63	1.12	25.98
L4	1.34	-0.31	1.21	0.56	9.95	17.58
DS7	9.77	-4.34	3.21	0.66	48.71	34.94
DS8	1.52	-1.74	-3.1	-2.85	-27.22	35.02
DS9	6.22	0.83	0.89	1.2	1.87	52.23

4. Conclusion

In this research, Fe_{0.7}Cr_{1.3}O₃ brown cool nano pigments were synthesized via the hydrothermal method. The XRD results demonstrated that the single-phase Fe_{0.7}Cr_{1.3}O₃ was synthesized at an optimum temperature of 800 °C. The succinic acid significantly affected the morphology of the synthesized particles. The optimum amount of succinic acid (2.63 wt%) increased (15 %) in IR reflectance compared to the reference sample. The sample with flaky particles showed the best performance in IR reflectance. The thickness of the flakes was smaller than 100 nm.

The effect of adding TEOS as a silica source during the synthesis process was also investigated. TEM, XRD, and FTIR results demonstrated that silica has

formed on the particles as a coating instead of being dispersed individually as silica particles. The highest reflectance (52 %) was observed in the DS9 sample, synthesized using 1.875 wt% TEOS and 2.63 wt% succinic acids because of the particles' flaky morphology and the difference between the reflecting indices of the silica layer and Fe_{0.7}Cr_{1.3}O₃ particle. Furthermore, silica provided a meaningful increase in IR reflectance of the base pigment and caused a decrease in the accumulation of the particles.

Acknowledgment

The authors appreciate the partial support of the Institute for Color Science and Technology and Malayer University.

5. References

1. C. Chen, A. Han, M. Ye, J. Wang, X. Chen, A new thermal insulation ceramic pigment: Ce doped $\text{Y}_3\text{Al}_5\text{O}_{12}$ compounds combined with high near-infrared reflectance and low thermal conductivity, *J. Alloys Compd.*, 886(2021), 161257.
2. W. Zhou et. al., Synthesis and characterization of novel yellow-green Al-doped $\text{Y}_3\text{Fe}_5\text{O}_{12}$ nano-pigments with high NIR reflectance, *J. Alloys Compd.*, 896(2021), 162883.
3. M. Tian et. al., Near-infrared reflectance and thermal insulating performance of Mo-doped Bi_2WO_6 with 3D hierarchical flower-like structure as novel ceramics pigment, *Ceram. Int.*, 46(2020), 12566-12573.
4. G. Yang et al., Sodium tungsten bronze (Na_xWO_3)-doped near-infrared-shielding bulk glasses for energy-saving applications, *J. Mater. Sci. Technol.*, 89(2021), 50-157.
5. S. Jose, S. B. Narendranath, D. Joshy, N. V Sajith, M. R. P. Kurup, P. Periyat, Low-temperature synthesis of NIR reflecting bismuth-doped cerium oxide yellow nano-pigments, *Mater. Lett.*, 233(2018), 82-85.
6. R. Levinson, P. Berdahl, H. Akbari, Solar spectral optical properties of pigments-Part II: a survey of common colorants, *Sol. Energy Mater. Sol. Cells*, 89(2005), 351-389.
7. S. D. Doli, D. J. Jovanovi, D. Trbac, L. A. Anin Far, M. D. Dami Anin, Improved coloristic properties and high NIR reflectance of environment-friendly yellow pigments based on bismuth vanadate, *Ceram. Int.*, 44(2018), 22731-22737.
8. L. Yuan, A. Han, M. Ye, X. Chen, C. Ding, L. Yao, Synthesis and characterization of novel nontoxic $\text{BiFe}_{1-x}\text{Al}_x\text{O}_3$ /mica-titania pigments with high NIR reflectance, *Ceram. Int.*, 43(2018), 16488-16494.
9. W. Zhou et. al., High near-infrared reflectance orange pigments of Fe-doped $\text{La}_2\text{W}_2\text{O}_9$: preparation, characterization, and energy consumption simulation, *ACS Sustainable Chem. Eng.*, 9(2021), 12385-12393.
10. J. Wang, A. Han, M. Ye, C. Chen, X. Chen, X. Zhu, Thermal Insulation Performance of Novel Coated Fabrics Based on Fe-Doped BaSnO_3 Near-Infrared Reflectance Pigments, *ACS Sustainable Chem. Eng.*, 9(2021), 16328-16337.
11. W. Zhou et. al., High near-infrared reflective $\text{Zn}_{1-x}\text{A}_x\text{WO}_4$ pigments with various hues facilely fabricated by tuning doped transition metal ions ($\text{A}=\text{Co}$, Mn , and Fe), *Inorg. Chem.*, 61(2022), 693-699.
12. P. Jeevanandam, R. S. Mulukutla, M. Phillips, S. Chaudhuri, L. E. Erickson, K. J. Klabunde, Near-infrared reflectance properties of metal oxide nanoparticles, *J. Phys. Chem. C*, 111(2007), 1912-1918.
13. N. Kiomarsipour, R. S. Razavi, K. Ghani, M. Kioumarsipour, Evaluation of shape and size effects on optical properties of ZnO pigment, *Appl. Surf. Sci.*, 270(2013), 33-38.
14. S. Ge et al., Self-assembled flower-like antimony trioxide microstructures with high infrared reflectance performance, *J. Solid State Chem.*, 200(2013), 136-142.
15. S. Soumya et al., Near IR reflectance characteristics of PMMA/ ZnO nanocomposites for solar thermal control interface films, *Sol. Energy Mater. Sol. Cells.*, 125(2014), 102-112.
16. T. Thongkanluang, T. Kittiauchawal, P. Limsuwan, Preparation and characterization of Cr_2O_3 - TiO_2 - Al_2O_3 - V_2O_5 green pigment, *Ceram. Int.*, 37(2011), 543-548.
17. T. Thongkanluang, P. Limsuwan, P. Rakkwamsuk, Preparation and application of high near-infrared reflective green pigment for ceramic tile roofs, *Int. J. Appl. Ceram. Technol.*, 8(2011), 1451-1458.
18. R. Levinson et al., Methods of creating solar-reflective nonwhite surfaces and their application to residential roofing materials, *Sol. Energy Mater. Sol. Cells*, 91(2007), 304-314.
19. V. C. Malshe, A. K. Bendiganavale, Infrared reflective inorganic pigments, *Recent Patents Chem. Eng.*, 1(2008), 67-79.
20. S. Sadeghi-Niaraki, B. Ghasemi, E. Ghasemi, M. Ghahari, Preparation of $(\text{Fe}, \text{Cr})_2\text{O}_3@ \text{TiO}_2$ cool pigments for energy-saving applications, *J. Alloys Compd.*, 779(2019), 367-379.
21. J. Zou, T. Zhang, and X. He, Dark brown Cr doped CaTiO_3 pigments with high NIR reflectance, *Mater. Lett.*, 248(2019), 173-176.
22. L. Liu, A. Han, M. Ye, W. Feng, The evaluation of the thermal performance of cool coatings colored with high near-infrared reflective nano-brown inorganic pigments: magnesium doped ZnFe_2O_4 compounds, *Sol. Energy*, 113(2015), 48-56.
23. A. Han, Y. Zhou, M. Ye, S. Feng, H. Du, R. Yang, Near-infrared reflectance and thermal performance of $\text{Na}_2\text{V}_6\text{O}_{16} \cdot x\text{H}_2\text{O}$ nanoribbon as a novel cool brown pigment, *Dye. Pigment.*, 123(2015), 242-247.
24. K. J. Park, D. S. Seo, W. Y. Jang, J. K. Lee, Effect of surfactant on the morphology of silver nanoparticles, *Solid State Phenomena*, 124(2007), 1205-1208.
25. S. Y. Moon, T. Kusunose, T. Sekino, CTAB-assisted synthesis of size- and shape-controlled gold nanoparticles in SDS aqueous solution, *Mater. Lett.*, 63(2009), 2038-2040.
26. A. R. Tao, S. Habas, P. Yang, Shape control of colloidal metal nanocrystals, *Small*, 4(2008), 310-325.
27. T. Fujii, S. Kawasaki, A. Suzuki, T. Adschiri, High-speed morphology control of boehmite nanoparticles by supercritical hydrothermal treatment with carboxylic acids, *Cryst. Growth Des.*, 16(2016), 1996-2001.
28. H. Siddiqui, M. S. Qureshi, F. Z. Haque, Surfactant assisted wet chemical synthesis of copper oxide (CuO) nanostructures and their spectroscopic analysis, *Optik*, 127(2016), 2740-2747.

29. Q. Gao, X. Wu, Y. Fan, Q. Meng, Color performance and near-infrared reflectance property of novel yellow pigment based on Fe_2TiO_5 nanorods decorated mica composites, *Dye. Pigment.*, 146(2017), 537-542.
30. H. J. Kim, H. J. Lee, D. S. Kim, Hollow TiO_2 flake prepared from TiO_2 coated glass flake for solar heat protection and their thermal performance, *Mater. Des.*, 150(2018), 188-192.
31. P. M. Shirage, A. K. Rana, Y. Kumar, S. Sen, S. G. Leonardi, G. Neri, Sr-and Ni-doping in ZnO nanorods synthesized by a simple wet chemical method as excellent materials for CO and CO_2 gas sensing, *RSC Adv.*, 6(2016), 82733-82742.
32. J. Chandrappan, V. Khetan, M. Ward, M. Murray, G. Jose, Devitrification of ultrafast laser-plasma produced metastable glass layer, *Sci. Mater.*, 131(2017), 37-41.
33. M. Iacob *et al.*, Iron-chromium oxide nanoparticles self-assembling into smectic mesophases, *RSC Adv.*, 4(2014), 6293-6299.
34. M. Ghahari *et al.*, Synthesis of suitable SiO_2 Nnano particles as the core in core-shell nanostructured materials, *J. Nanosci. Nanotechnol.*, 11(2011), 5311-5317.
35. Y. S. Li, J. S. Church, A. L. Woodhead, F. Moussa, Preparation and characterization of silica-coated iron oxide magnetic nanoparticles, *Spectrochim. Acta Part A Mol. Biomol. Spectrosc.*, 76(2010), 484-489.
36. A. Sood, V. Arora, J. Shah, R. K. Kotnala, T. K. Jain, Multifunctional gold-coated iron oxide core-shell nanoparticles stabilized using thiolated sodium alginate for biomedical applications, *Mater. Sci. Eng. C*, 80(2017), 274-281.
37. V. Fang, J. V. Kennedy, J. Futter, J. Manning, *A review of near-infrared reflectance properties of metal oxide nanostructures*. GNS Science, 2013.
38. S. Son, S. H. Hwang, C. Kim, J. Y. Yun, J. Jang, Designed synthesis of $\text{SiO}_2/\text{TiO}_2$ core/shell structure as light scattering material for highly efficient dye-sensitized solar cells, *ACS Appl. Mater. Interfaces*, 5(2013), 4815-4820.
39. T. Thongkanluang, N. Chirakanphaisarn, P. Limsuwan, Preparation of NIR reflective brown pigment, *Procedia Eng.*, 32(2012), 895-901.
40. M. Khajeh Aminian, T. Azizi, R. Dehghan, M. Hakimi, Synthesis and characterization of CoAl_2O_4 nano pigments by polyol method, *Prog. Color. Color. Coatings*, 10(2017), 231-238.

How to cite this article:

Gh. Mobarhan, A. Souri, S. K. Seyed Mostafavi, M. Ghahari, M. Safi, Synthesizing and Characterizing the Hybrid Pigment $\text{Fe}_{0.7}\text{Cr}_{1.3}\text{O}_3$ With High NIR Reflectance for Sustainable Energy Saving Applications. *Prog. Color Colorants Coat.*, 15 (2022), 341-353.

